Sulfur vacancy-rich tungsten disulfide and metal-organic framework derived Co$_3$O$_4$ heterostructure for sulfur ion degradation-assisted efficient hydrogen production

Ranjith Kumar Dharman [a1], Athibala Mariappan[a1], Pandian Mannu[b], Ta Thi Thuy Nga[b], Chung-Li Dong*[b], Tae Hwan Oh[a]*

a School of Chemical Engineering, Yeungnam University, Gyeongsan, 38541, South Korea

b Department of Physics, Tamkang University, New Taipei City 25137, Taiwan

[1]*These authors contributed equally*

Corresponding author mail id:

T.H.O *(taehwanoh@ynu.ac.kr)*

C.L.D *(cldong@mail.tku.edu.tw)*

Chemicals

All chemicals were of analytical grade and were used as received. Sodium tungstate dihydrate ($H_4Na_2O_6W$, 98–100%), thiourea (CH_4N_2S, 96%), oxalic acid ($C_2H_2O_4$, 98.5%), cobalt(II) nitrate hexahydrate ($Co(NO_3)_2$, ~97%), 2-methylimidazole ($C_4H_6N_2$, ~98%), methanol (CH_3OH, ~99.99%), and ethanol (C_2H_5OH, 94%) were purchased from Daejung Chemicals. Carbon cloth (CC) was commercially obtained from NARA Cell-Tech Corporation and employed as the substrate for the working electrode.

Electrochemical measurements

All electrochemical experiments were conducted using a Corrtest workstation (CS350 in COM3) with a three-electrode setup. The tests were performed using 1 M KOH and (1 M KOH + 1 M Na_2S) as electrolyte solutions for the water and sulfur oxidation reactions (OER, HER, and SOR). The catalyst ink for the working electrode was prepared by grinding the catalyst material, acetylene black, and polyvinylidene fluoride (PVDF) in a ratio of 80:10:10 using N-methyl-2-pyrrolidone (NMP) as the solvent. The as-prepared catalyst ink coated on CC (1 cm^2), a platinum plate, and Hg/HgO were used as the working, counter, and reference electrodes, respectively. The linear sweep voltammetry (LSV) curves were obtained within different voltage windows for the HER, OER, and SOR at a scan rate of 5 mV s^{-1} with 85 % iR-compensation. The overpotential (η) and Tafel slope were calculated using the equations: $\eta = E_{RHE} - 1.23$ (OER) and $\eta = b \log(j) + a$ (where j is the current density and b is the Tafel slope). Electrochemical impedance spectroscopy (EIS) data were acquired in the frequency range of 100 kHz to 0.1 Hz with an amplitude of 10 mV. The double-layer capacitance (C_{dl}) and electrochemical surface area (ECSA) were calculated from the CV curves acquired in the non-Faradaic region at different

scan rates from 20 to 100 mV s^{-1}. The corresponding ECSA was calculated using the following equation: ECSA = Cdl/C_s, where C_s is the specific capacitance of the sample (C_s = 0.040 mF cm^{-2}) in 1 M KOH electrolyte [1]. The catalyst stability was evaluated via chronopotentiometry measurement at a current density of 10 mA cm^{-2}. The overall water-splitting performance was evaluated in a two-electrode cell using the CW-2 electrocatalyst as both the anode and cathode. Moreover, the stability during the operation of a full cell was explored by chronopotentiometry measurement at 10 mA cm^{-2}. All the potentials were calibrated relative to the reversible hydrogen electrode (RHE) according to the Nernst equation: E_{RHE} = $E_{Hg/HgO}$ + 0.059 × pH + 0.098. Furthermore, a two-cell configuration for the SOR was achieved by assembling the CW-2 catalysts as the anode and cathode in an H-type electrolyzer.

Turnover frequency

Turnover frequency (TOF) values can be calculated from the formula; TOF (s^{-1}) = $j \times N_A/(n \times S_A \times F)$, where, j is the current density, N_A is the Avogadro's number, n is the number of electrons involved to produce one molecule of the product (in case of UOR; 6 electrons are involved to produce O_2 molecule), F is the Faraday constant, and S_A is the amount of accessible active sites. The S_A is calculated from the formula; S_A = (Integrated area of reduction part of CV curve/scan rate)/charge of an electron.

Faradic efficiency measurement and calculation:

Faradaic measurements of the catalysts were conducted using the chronopotentiometry technique, maintaining a constant current density of 10 mA cm^{-2}. The generated O_2 gas from the working electrode was monitored at 10-minute intervals. Subsequently, the following calculations were employed:[61]

$$\text{Faradaic efficiency} = \frac{Experimental\ \mu mol\ of\ O_2\ gas}{Theoretical\ \mu mol\ of\ O_2\ gas} \times 100$$

The theoretical µmol of O_2 gas was calculated from Faraday's law;

$$n = \frac{I \times t}{z \times F}$$

, where n is the number of mol, I is current (A), t is time (s), z is the transfer of electrons ($z = 4$), and F is the Faraday constant (96,485 C mol^{-1}).

The experimental µmol of O_2 gas was measured from the water displacement method and then the pressure is converted into units of an atmosphere by Dalton's law of partial pressure

$$P_{total} = P_{oxygen} + P_{water}$$

The number of µmol of O_2 gas produced in water displacement is calculated by,

$$PV = nRT$$

Where, V is the volume of produced gas (liters), T is the temperature (kelvin), and R is the ideal gas constant (0.0821 L atm/mol K).

Calculation of SOR Faradic efficiency:

The mass of sulfur powder (m_s) was obtained from the acidification process after the chronopotentiometric test. The Faradic efficiency of sulfur is calculated using ;

$$Faradic\ efficiency = \frac{m_s \times Z \times F}{M_s \times Q} \times 100\%$$

Where m_s denotes the weight of sulfur, M_s denotes the relative molecular weight of sulfur, Z denotes the number of electrons producing a sulfur molecule, F is the Faraday constant (96,45 C mol^{-1}), and Q is the recorded charge during the electrolysis.

Characterization

The X-ray diffraction (XRD, Xpert Pro equipped with Cu Kα radiation) was used to study the crystal structures of the samples. Field emission scanning microscopy (FE-SEM, HITACHI S-4800 and high-resolution transmission electron microscopy (HRTEM, Titan G2 ChemiSTEM Cs Probe) was used to analyze the morphological nature of the obtained materials. The electronic properties and chemical surface analysis were studied by X-ray photoelectron spectroscopy (XPS, Thermoscientific K-α surface analysis). The electron spin resonance spectra were measured using an electron spin resonance spectrometer (Brucker (EMXplus-9.5/2.7)).

X-Ray Absorption Spectroscopy Characterization

The synchrotron X-ray absorption spectroscopy (XAS) analysis were conducted at the Taiwan Light Source (TLS), a part of the National Synchrotron Radiation Research Center (NSRRC), Taiwan, on beamline BL17C, which was fitted with a Si (111) double-crystal monochromator. The TLS storage ring ran at 1.5 GeV and a current of 360 mA. There were two distinct zones of XAS, and the X-ray absorption near-edge structures (XANES) were at the absorption edge of the XAS spectrum between −30 and 100 eV. The oxidation state and band occupancy were determined based on the binding energy of a core electron. The extended X-ray absorption fine structures (EXAFS), which were oscillations within the region beyond the absorption edge of 50 eV to 1000 eV, were linked to the local electronic structure such as coordination numbers, bond

distances, as well as Debye-Waller factors. These could be produced by electron backscatter by atoms in the surrounding coordination environment. Both the W and Co K-energy edges resolutions were adjusted to 0.35 eV. Transmission mode was used to record the XAS spectra. Standard techniques were used to examine the raw data, including data prior to and after edge background subtractions, edge jump normalization, and Fourier processing.

In Situ X-Ray Absorption Spectroscopy Characterization

X-ray absorption spectroscopy (XAS) studies were carried out at beamline BL17C (at the Taiwan Light Source (TLS), National Synchrotron Radiation Research Center (NSRRC), Taiwan). The XAS spectra were collected in transmission mode. In-situ XAS was carried out at BLO1C (NSRRC) by fluorescence mode. Raw data were analyzed following standard procedures, including pre-edge and post-edge background subtractions, normalization for the edge jump, and Fourier transformation.
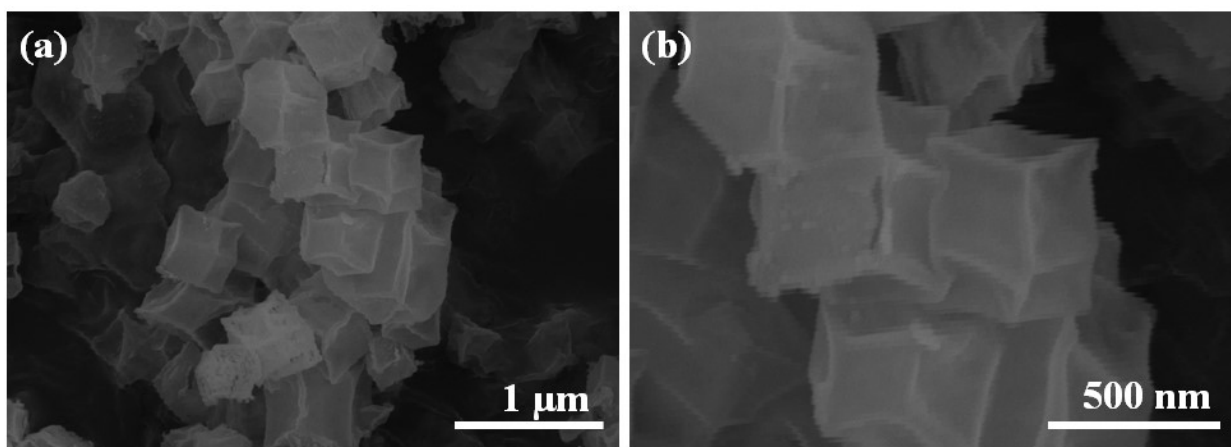
Fig. S1. (a,b) FESEM images of MOF-derived Co_3O_4 catalyst.
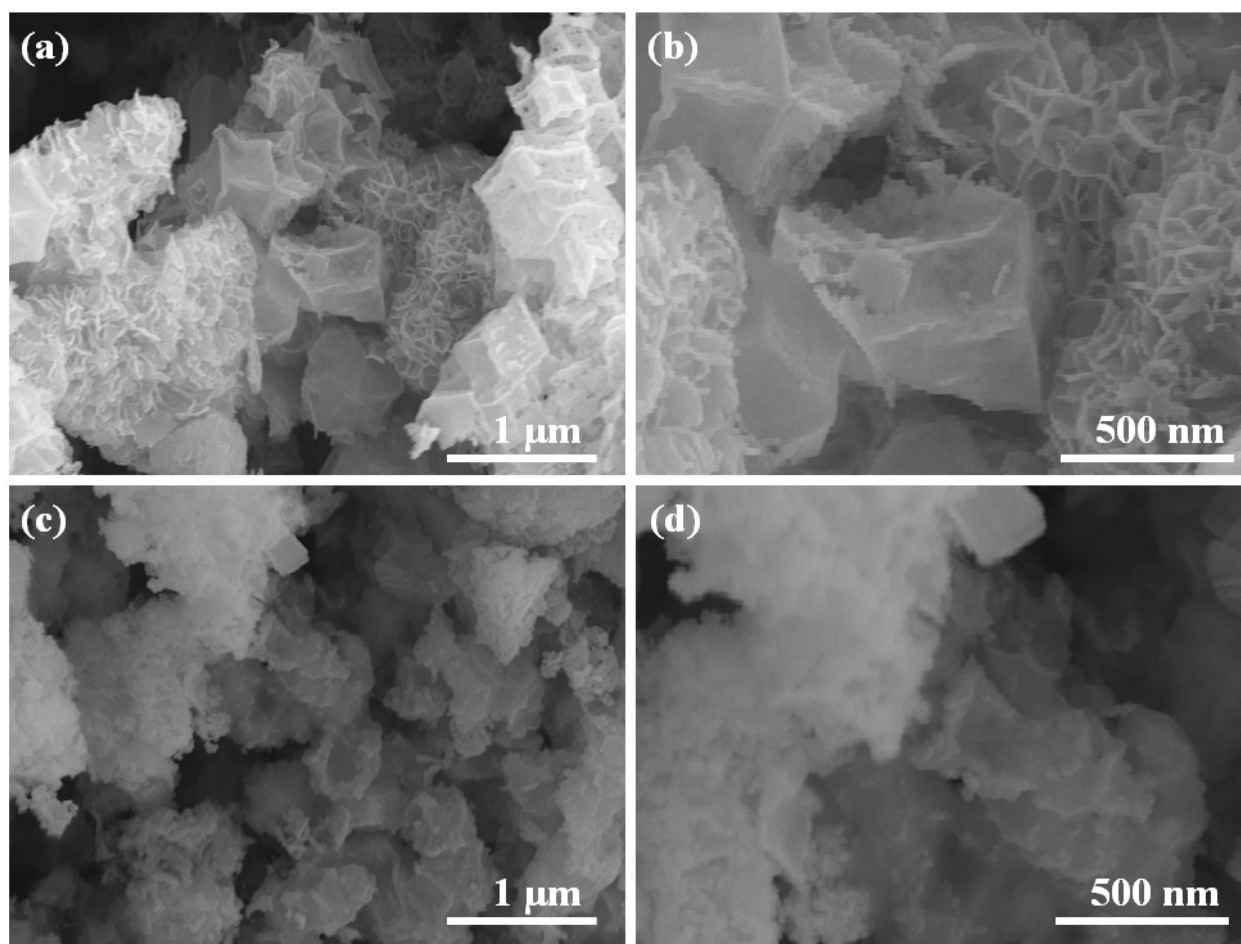
Fig S2. FESEM images of (a,b) CW-1 and (c,d) CW-3 heterostructure samples.
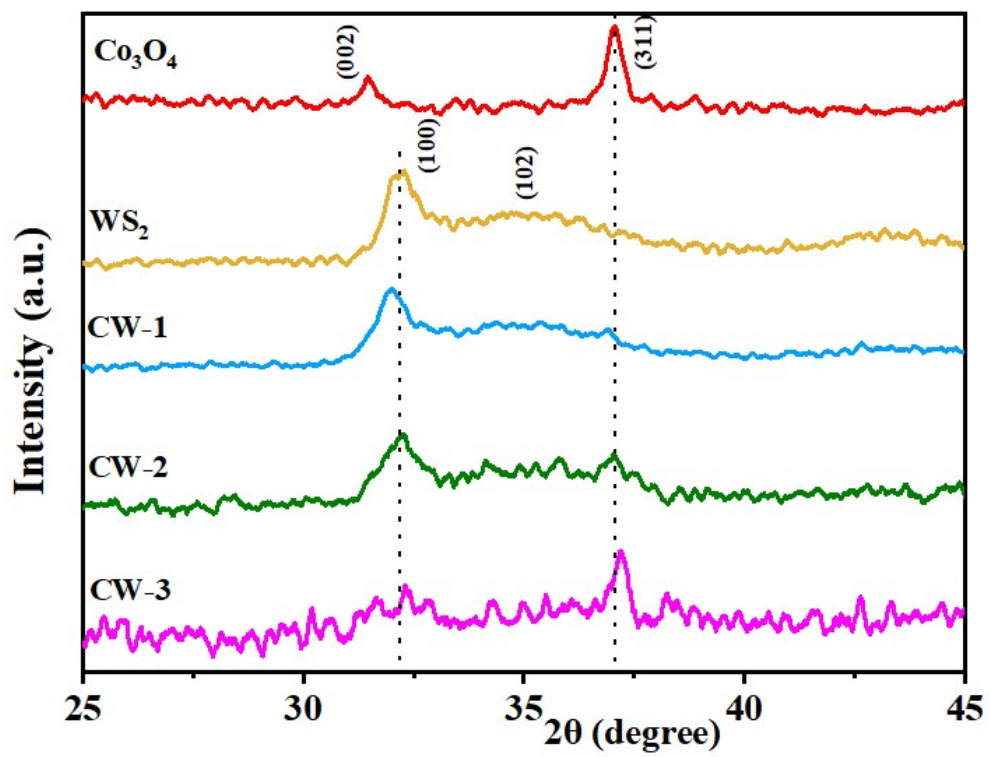
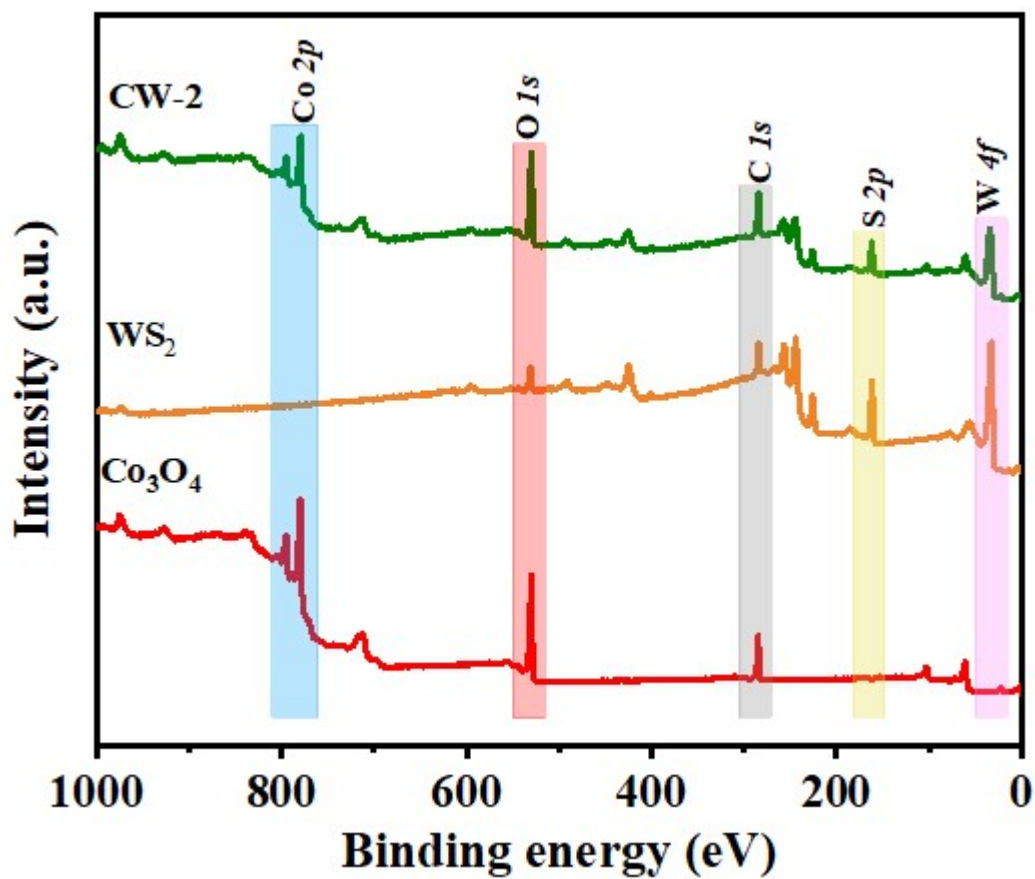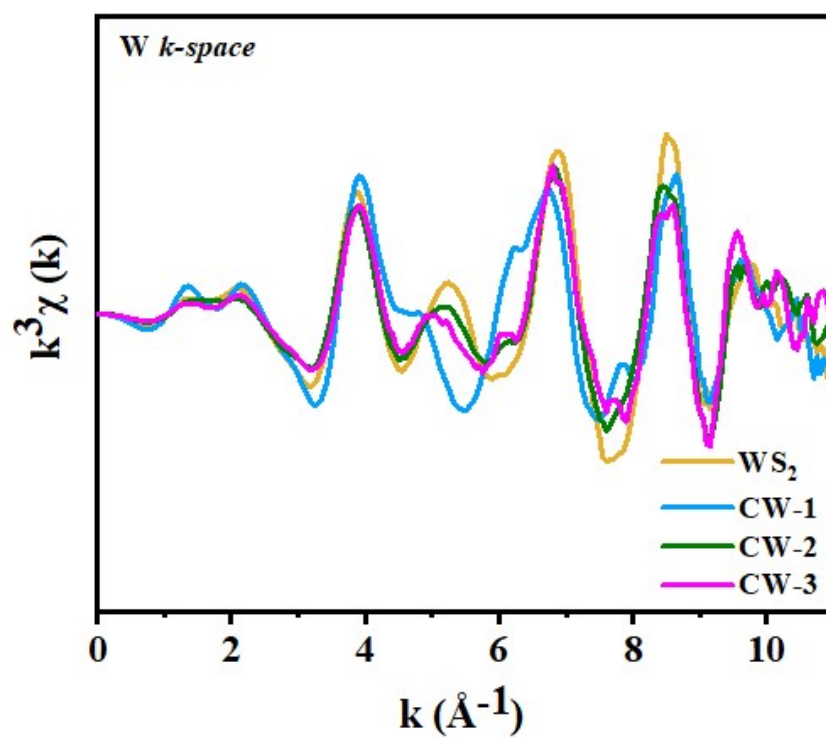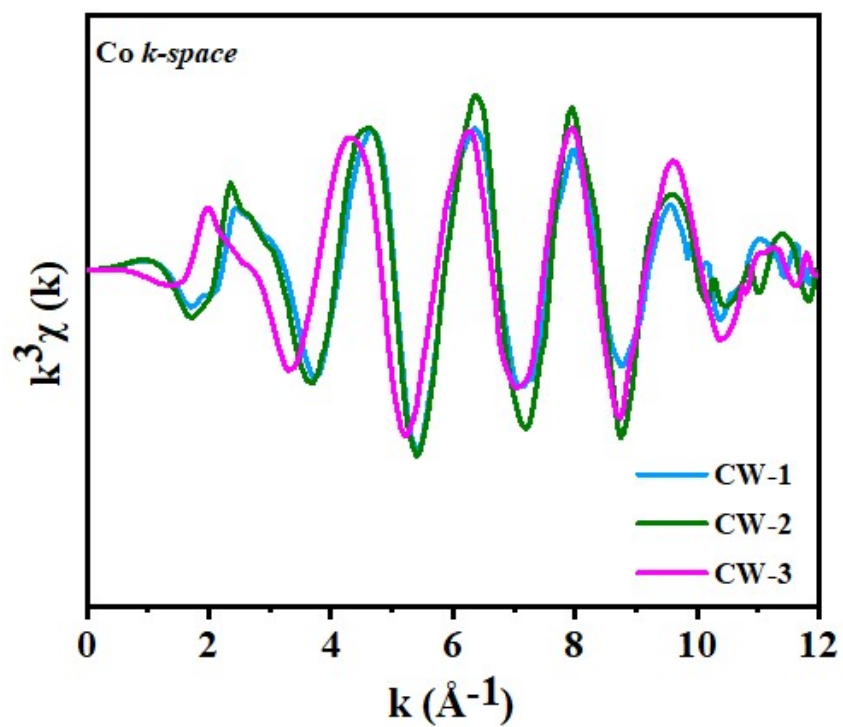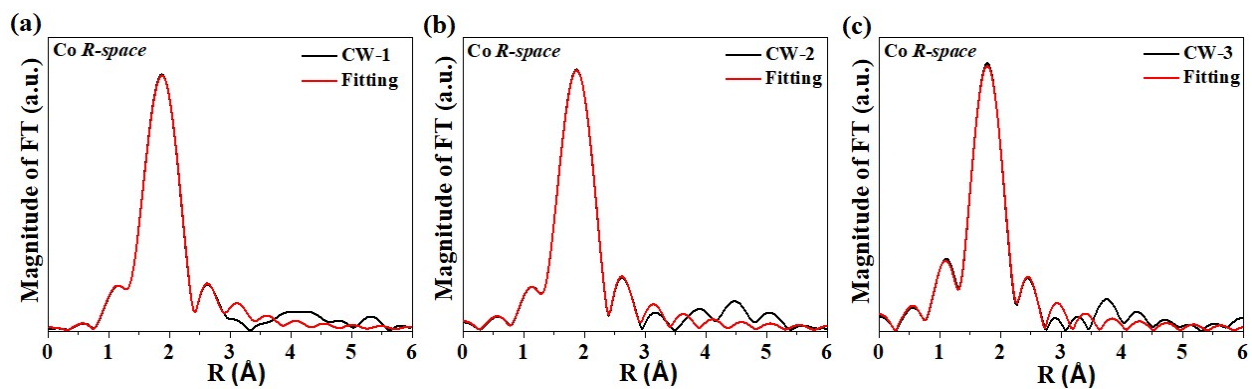**Fig S3.** Enlarged XRD pattern of different electrocatalysts.

**Fig S4.** XPS survey spectrum of WS_2, Co_3O_4, and CW-2 catalysts.

Fig S5. Fourier-transformed $k^3\chi$ data of EXAFS oscillations for W *k-space* of different catalysts.
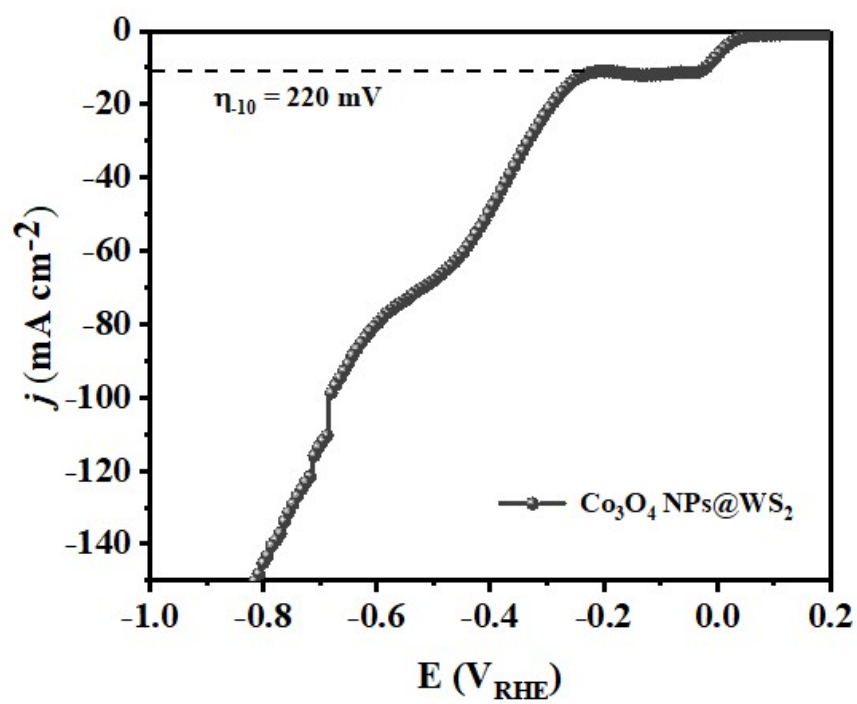
Fig S6. Fourier-transformed $k^3\chi$ data of EXAFS oscillations for Co *k-space* of different catalysts.
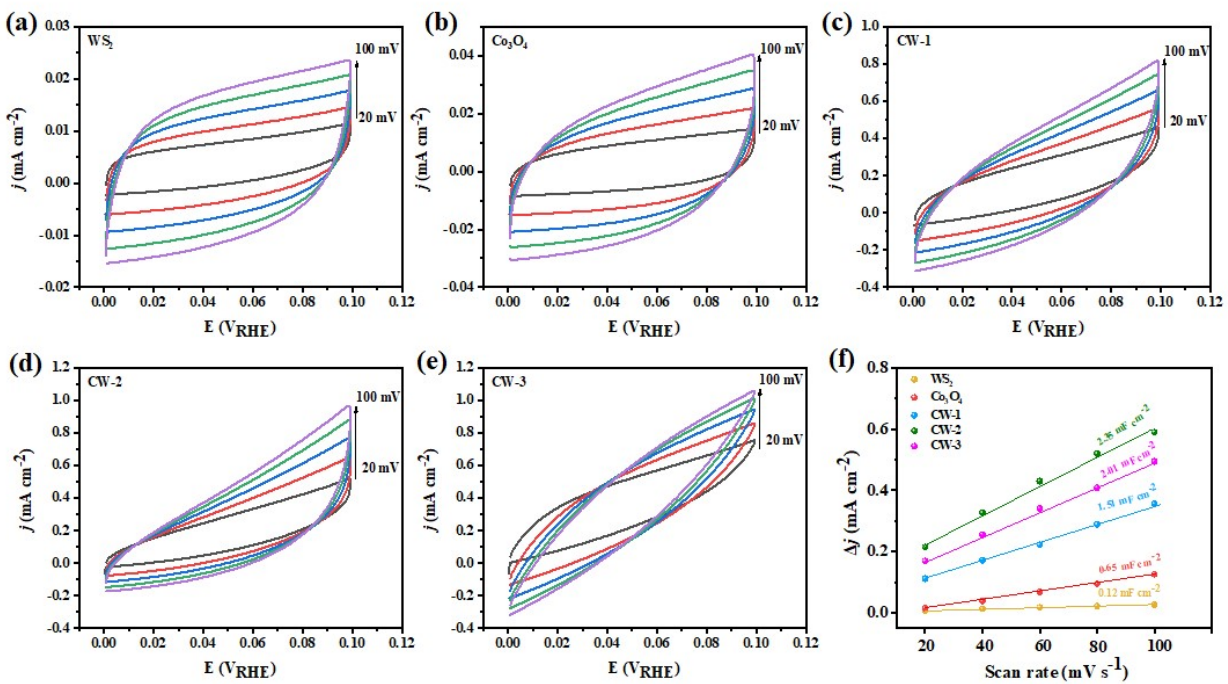
Fig. S7. EXAFS spectra of prepared heterostructure catalysts and the corresponding fitting results for CW-1 (a), CW-2 (b), and CW-3 (c). Experimental data and fitted profiles are highlighted as black and red lines, respectively.
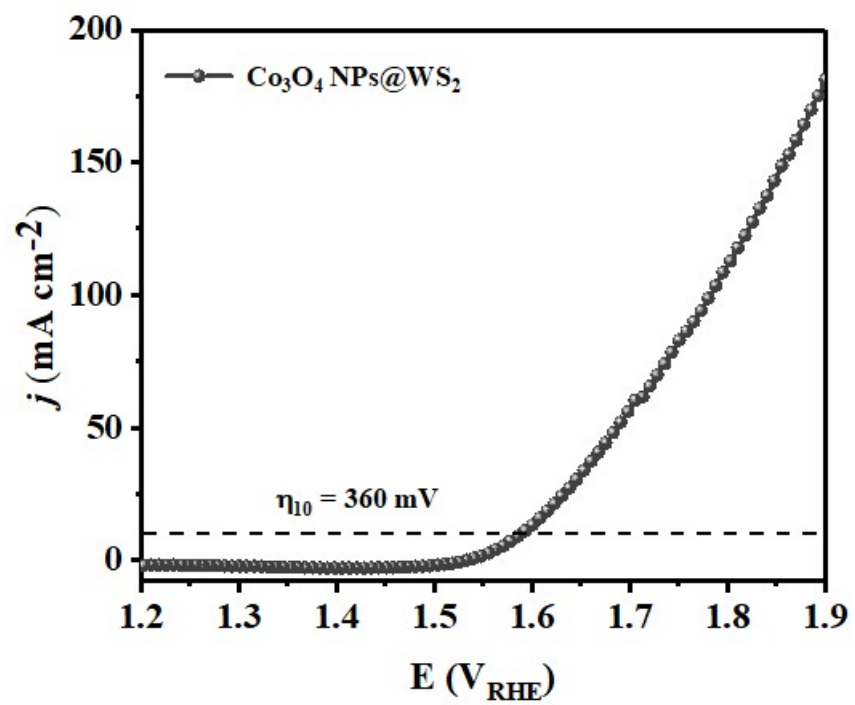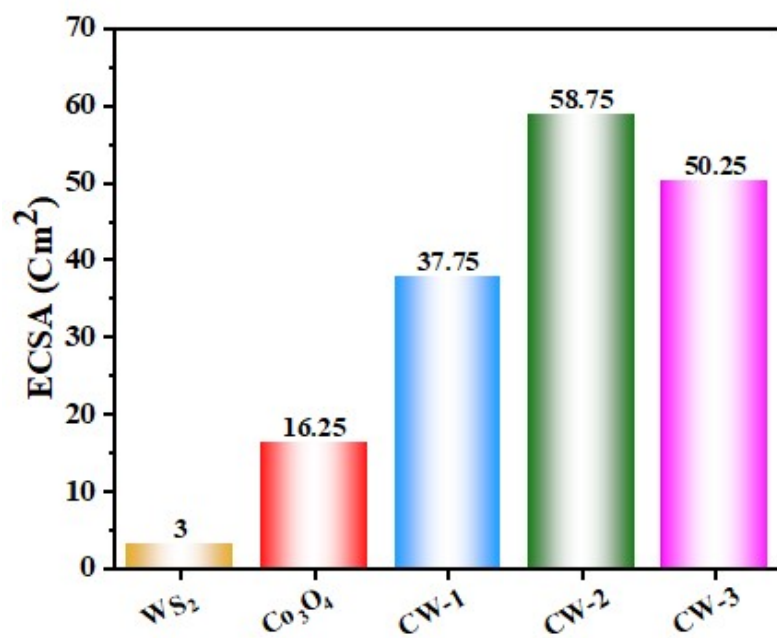
Fig S8. OER polarization curve of Co_3O_4 NPs@WS_2.

Fig S9. HER polarization curve of Co_3O_4 NPs@WS$_2$.

Fig S10. (a-e) CV spectra of different catalysts and (f) C_{dl} plots of different electrocatalysts.

Fig. S11. ECSA of different catalysts.
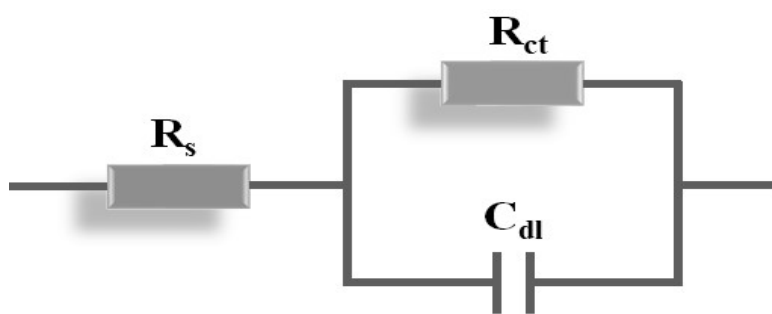
Fig S12. Equivalent circuit for fitting EIS data obtained for OER, HER, and SOR.
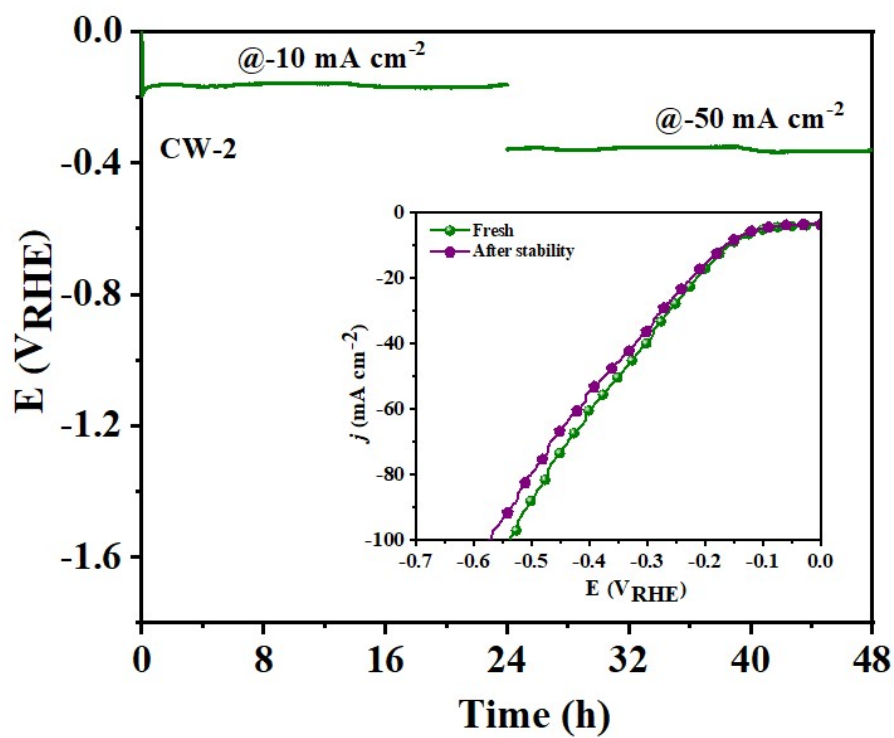
Fig. S13. Chronopotentiometric curve of CW-2 at -10 and -50 mA cm^{-2} (inset shows LSV curve of CW-2: initial and after 48 h).
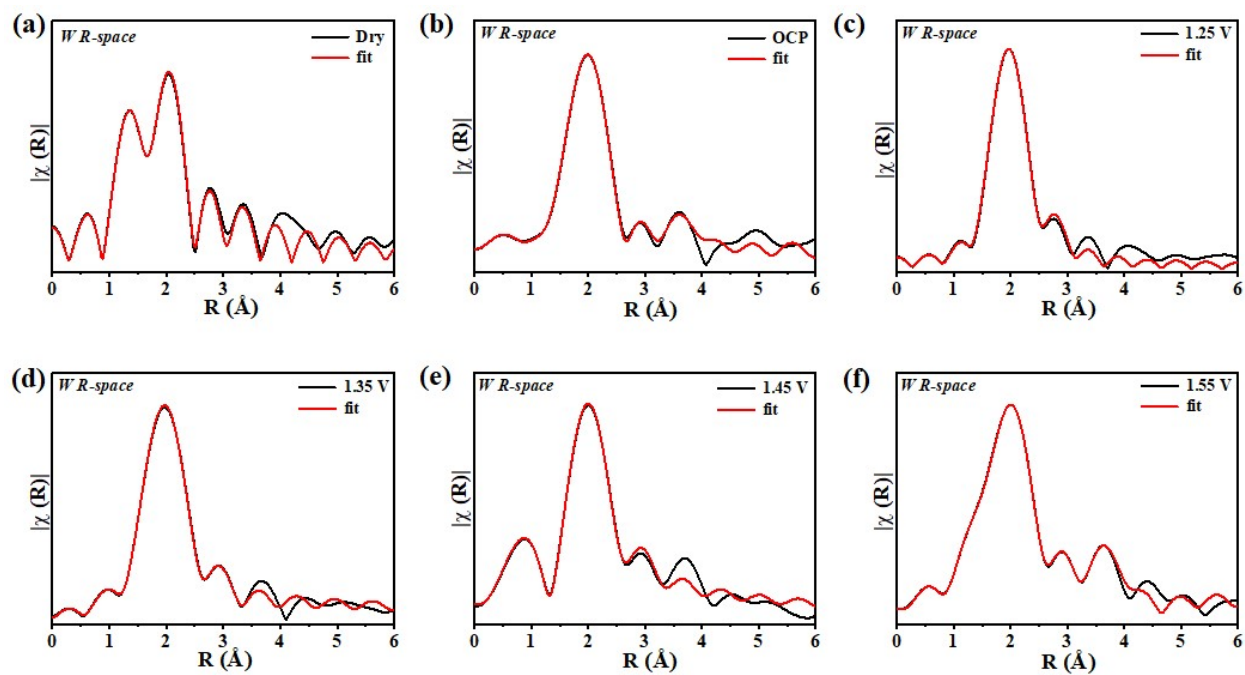
Fig. S14. (a-f) The fitting results of W L3-edge EXAFS spectra at OCP to 1.55 V applied potential.
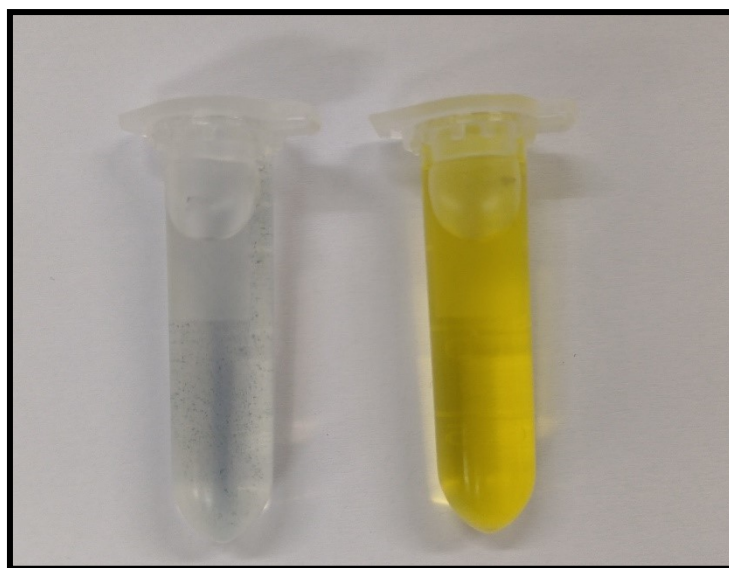
Fig. S15. Photographic image of colorimetric changes of SOR.
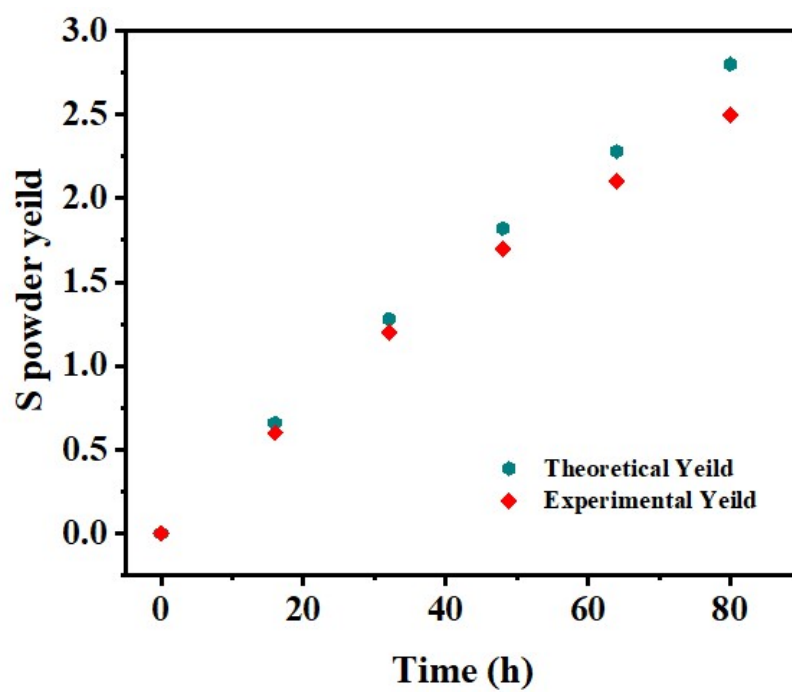
Fig. S16. Theoretical and experimental yield of sulfur powder at the anode during the electrolysis.
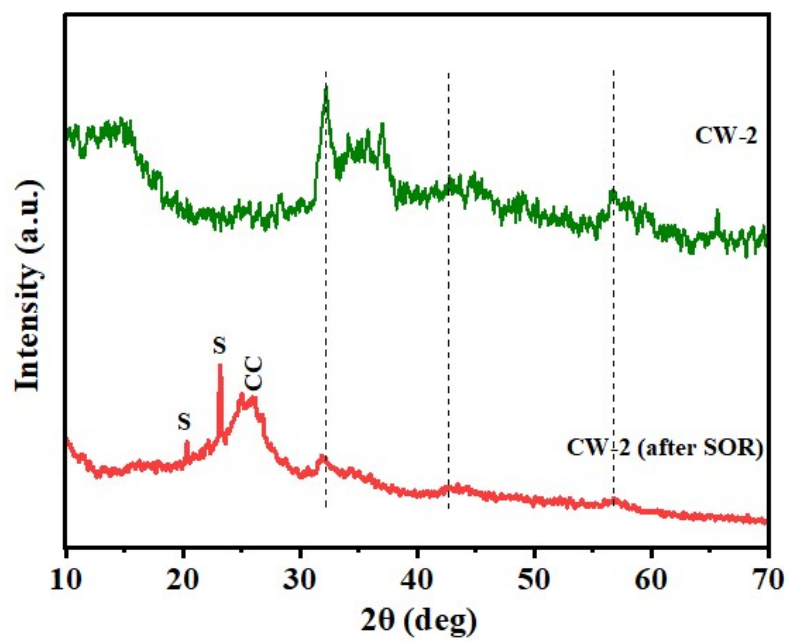
Fig. S17. XRD pattern of CW-2 and CW-2 (after SOR stability).
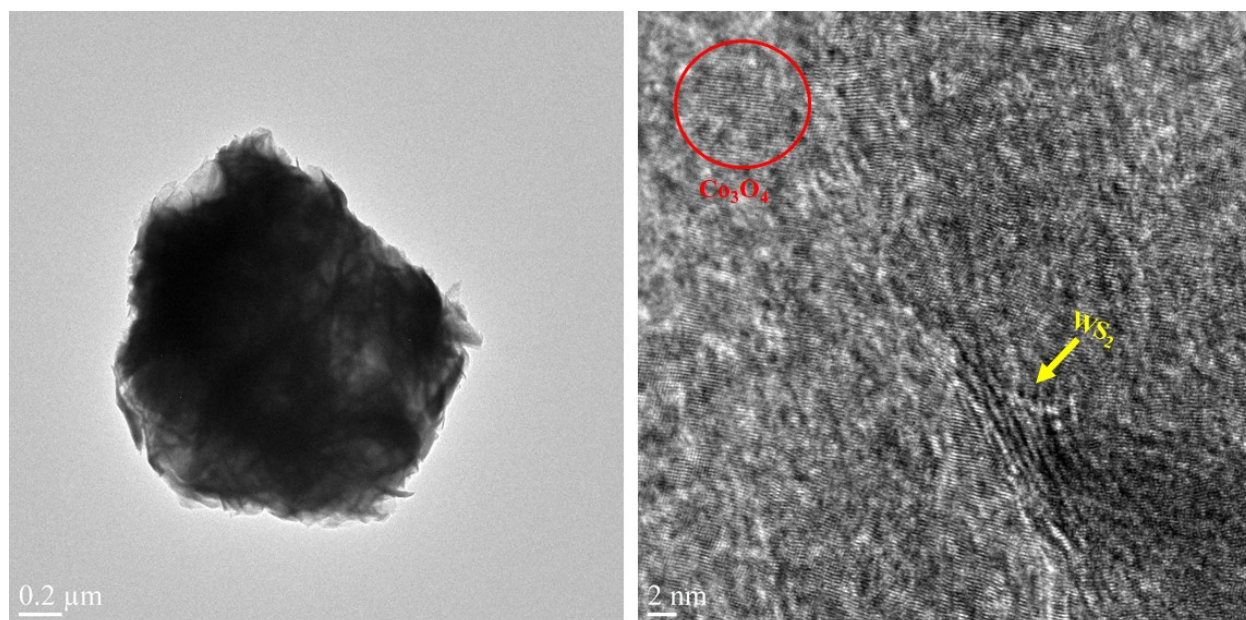
Fig. S18. HRTEM image of CW-2 (after SOR stability).
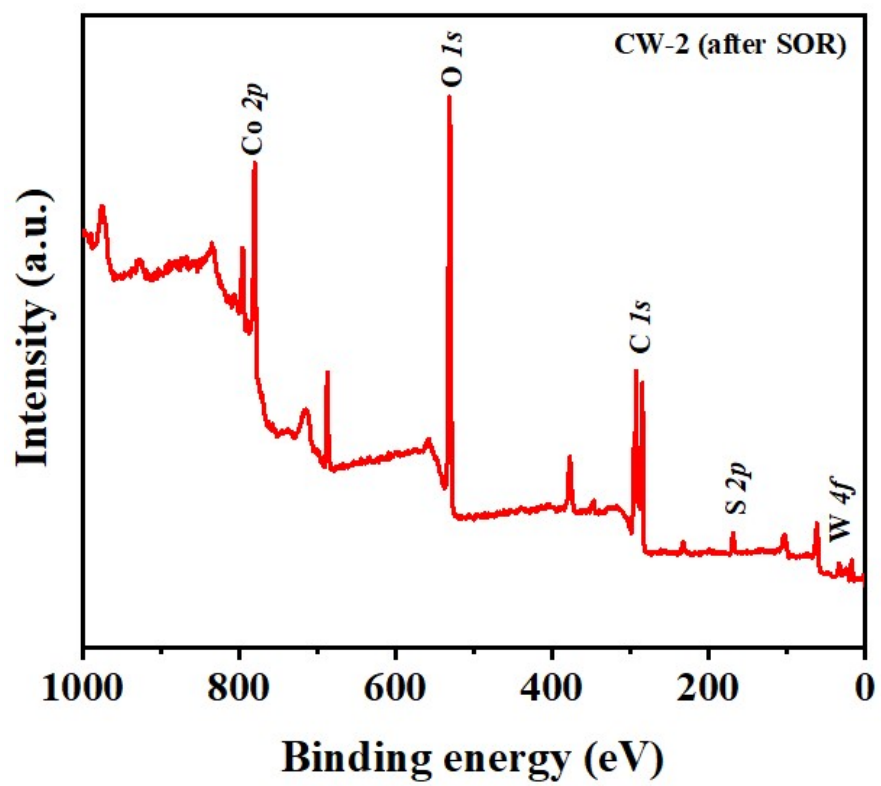
Fig. S19. XPS survey spectra of CW-2 (after SOR stability).
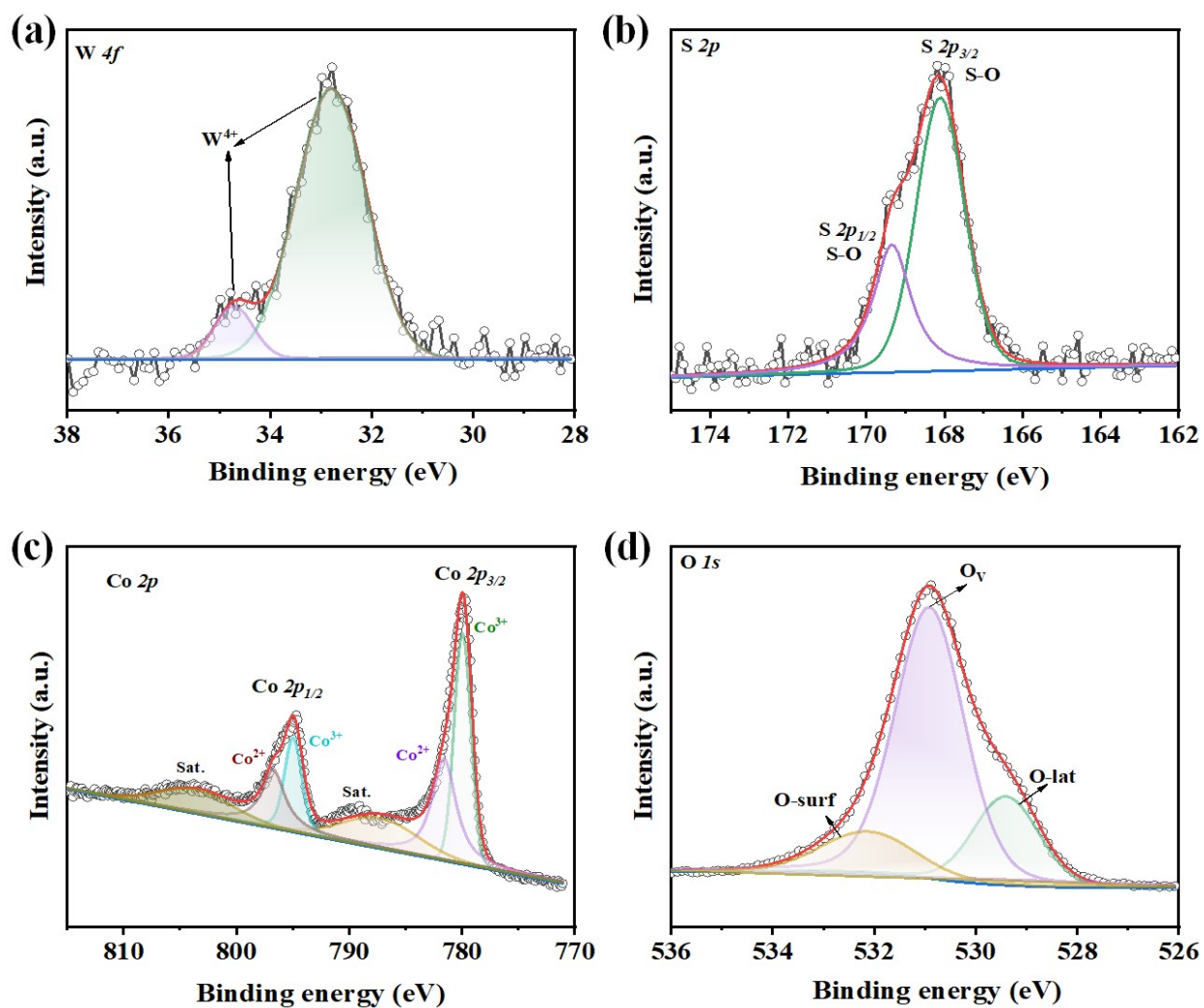
Fig. S20. High-resolution XPS spectra (a) W 4f, (b) S 2p, (c) Co 2p, and (d) O 1s spectra of CW-2 (after SOR stability).

Table S1. Summary of FT-EXAFS fitting data for CW at critical potential.

Samples	Path	CN= N × S_0^2	σ^2 (Å^{-2})	ΔE_0 (eV)	R-factor	R(Å)
CW-1	Co-O/S	5.61	0.0086	-12.92	0.0014	2.19
	Co-Co	4.95	0.0107	-74.32		2.53
CW-2	Co-O/S	5.43	0.0001	-19.25	0.0007	1.99
	Co-Co	4.21	0.0001	-99.03		2.48
CW-3	Co-O/S	5.22	0.0132	-10.104	0.0023	2.00
	Co-Co	4.55	0.0043	-94.78		2.47

Table S2. Summary of previously reported TMDs-based heterostructure HER electrocatalysts towards the three-cell electrode.

Catalyst	Electrolyte	HER Overpotential (mV) @ 10 mA cm^{-2}	Ref
ZnS-ZnO-MoS$_2$/Ti$_3$C$_2$T$_x$	0.5 M H$_2$SO$_4$	327	[2]
1T/2H MoS$_2$/Ti$_3$C$_2$T$_x$	1 M KOH	300	[3]
MoS$_2$/Graphene	1 M KOH	183	[4]
NiCo-WSe$_2$	0.5 M H$_2$SO$_4$	205	[5]
MoS$_2$/Black Phosphorus	1 M KOH	237	[6]
Ag/MCNT/WS$_2$	1 M KOH	218	[7]
S doped-WTe$_2$	1 M KOH	195	[8]
CoSe$_2$@N-doped rGO	0.5 M H$_2$SO$_4$	172	[9]
P-doped@1T- WS$_2$	1 M KOH	190	[10]

Ni@N-Gr/MoS$_2$	0.5 M H$_2$SO$_4$	270	[11]
MoSe$_2$-Mo$_2$C/NC	1 M KOH	214	[12]
MOF-derived Co$_3$O$_4$@WS$_2$	**1 M KOH**	**153**	**This work**

Table S3. Summary of previously reported TMDs-based heterostructure OER electrocatalysts towards the three-cell electrode.

Catalyst	Electrolyte	OER Overpotential (mV) @ 10 mA cm^{-2}	Reference
MoSe$_2$@CoAl-LDH	1 M KOH	360	[13]
NiMoSe@Ti$_3$C$_2$T$_x$	1 M KOH	320	[14]
FeNi@N-doped Mo$_2$C	1 M KOH	304	[15]
MoSe$_2$@Co/Ni NPs	1 M KOH	378	[16]
Ni(OH)$_2$/MoS$_2$	1 M KOH	360	[17]
N-doped MoS$_2$@CoFe NPs	1 M KOH	337	[18]
CoTe$_2$/NiTe$_2$@ N-doped NCBs	1 M KOH	320	[19]
MoS$_2$/NiS$_2$	1 M KOH	303	[20]
Fe$_2$O$_3$-MnO	1 M KOH	370	[21]
MOF-derived WS$_2$@Co$_3$O$_4$	**1 M KOH**	**270**	**This work**

Table S4. Summary of FT-EXAFS fitting data for CW-2 at critical potential.

Samples	Path	CN= N × S_0^2	σ^2 (Å^{-2})	ΔE_0 (eV)	R-factor	R(Å)
CW-2 Air	W-S	5.41	0.00573	-6.734	0.0040	2.37
	W-W	3.13	0.03889	-5.836		2.98
CW-2 OCP	W-S	5.57	0.01116	-4.123	0.0041	2.39
	W-W	3.22	0.01480	-5.146		3.03
CW-2 0.25 V	W-S	5.71	0.01828	-6.016	0.0022	1.963
	W-W	3.35	0.00231	-5.457		2.952
CW-2 0.35 V	W-S	5.82	0.02032	-6.201	0.0119	1.964
	W-W	3.49	0.00845	-5.707		2.957
CW-2 0.45 V	W-S	5.86	0.01163	-6.331	0.0701	1.965
	W-W	3.56	0.01657	-5.311		2.953
CW-2 0.55 V	W-S	5.75	0.01445	-6.247	0.0045	1.963
	W-W	3.68	0.02385	-5.258		2.953

N is the coordination number; S^2_0 is amplitude reduction factor, R is the interatomic distance (the bond length between X-ray absorbing atoms and surrounding coordination atoms); σ^2 is Debye-Waller factor (a measure of thermal and static disorder in absorber-scattered distances); E0, inner potential correction; R-factor, indicating the goodness of the fit.

Table S5. Comparision of previously stated SOR electrocatalysts towards three and two -cell electrode.

Catalyst	Electrolyte	SOR Potential (V)	HER//SOR Potential (V)	Reference
Fe, F co-doped NiO	1 M KOH + 1 M Na$_2$S	0.63 @ 100 mA cm^{-2}	0.83 @ 100 mA cm^{-2}	[22]
FeMo-S@Ru	1 M NaOH + 2.4 M Na$_2$S	0.31 @ 100 mA cm^{-2}	0.57 @ 100 mA cm^{-2}	[23]
Cu@NiFe-LDH	1 M KOH + 1 M Na$_2$S	0.31 @ 100 mA cm^{-2}	0.61 @ 50 mA cm^{-2}	[24]
a-RhS$_{2-x}$ metallene	1 M KOH + 4 M Na$_2$S	0.48 @ 100 mA cm^{-2}	0.44 @ 10 mA cm^{-2}	[25]
CoS@MoS$_2$	1 M KOH + 1 M Na$_2$S	0.31 @ 10 mA cm^{-2}	0.52 @ 10 mA cm^{-2}	[26]
TPA@Ni$_3$S$_2$	1 M KOH + 1 M Na$_2$S	0.48 @ 100 mA cm^{-2}	-	[27]
V$_{Pd}$@Pd$_4$S	1 M KOH + 4 M Na$_2$S	0.77 @ 100 mA cm^{-2}	0.59 @ 100 mA cm^{-2}	[28]

NiS@CoS	1 M NaOH + 1 M Na$_2$S	0.34 @ 100 mA cm^{-2}	0.54 @ 100 mA cm^{-2}	[29]
Nano Ni functionalized@MoS$_2$	1 M NaOH + 1 M Na$_2$S	0.35 @ 10 mA cm^{-2}	0.49 @ 10 mA cm^{-2}	[30]
MOF-derived WS$_2$@Co$_3$O$_4$	**1 M KOH + 4 M Na$_2$S**	**0.31 @ 10 mA cm^{-2}**	**0.41 @ 10 mA cm^{-2}**	**This work**

References:

[1] A. Mariappan, R.K. Dharman, T.H. Oh, S. Prabu, K.-Y. Chiang, Silver nanoparticles embedded in phosphorus and nitrogen-doped hierarchical hollow porous carbon for efficient supercapacitor and electrocatalytic water oxidation, Colloids and Surfaces A: Physicochemical and Engineering Aspects, 671 (2023) 131579.

[2] F. Rasool, B.M. Pirzada, M. Misbah Uddin, M.I.H. Mohideen, I. Yildiz, M. Elkadi, A. Qurashi, Interfacial engineering of ZnS–ZnO decorated MoS2 supported on 2D Ti3C2Tx MXene sheets for enhanced hydrogen evolution reaction, International Journal of Hydrogen Energy, 59 (2024) 63-73.

[3] J.Y. Loh, F.M. Yap, W.-J. Ong, 2D/2D heterojunction interface: Engineering of 1T/2H MoS2 coupled with Ti3C2Tx heterostructured electrocatalysts for pH-universal hydrogen evolution, Journal of Materials Science & Technology, 179 (2024) 86-97.

[4] X. Yu, G. Zhao, S. Gong, C. Liu, C. Wu, P. Lyu, G. Maurin, N. Zhang, Design of MoS2/Graphene van der Waals Heterostructure as Highly Efficient and Stable Electrocatalyst for Hydrogen Evolution in Acidic and Alkaline Media, ACS Applied Materials & Interfaces, 12 (2020) 24777-24785.

[5] F.-b. Guo, X.-y. Zhao, H.-y. Lei, Y. Xu, K.-k. Liu, L.-x. Zhang, J.-m. Xue, H.-r. Sun, Bimetallic doping-derived heterostructures in NiCo-WSe2 to promote hydrogen evolution reaction, Journal of Alloys and Compounds, 924 (2022) 166538.

[6] T. Liang, Y. Liu, Y. Cheng, F. Ma, Z. Dai, Scalable Synthesis of a MoS2/Black Phosphorus Heterostructure for pH-Universal Hydrogen Evolution Catalysis, ChemCatChem, 12 (2020) 2840-2848.

[7] X. Ma, Z. Lin, T. Feng, G. Liu, Fabricating 0D/1D/2D Ag/Carbon Nanotube/WS2 Heterostructure for Boosted Hydrogen Evolution Reaction in Akaline and Acidic Conditions, Energy & Fuels, 37 (2023) 16824-16832.

[8] W. Lin, B. Zhang, J. Jiang, E. Liu, J. Sha, L. Ma, Anionic and Cationic Co-Substitutions of S into Vertically Aligned WTe2 Nanosheets as Catalysis for Hydrogen Evolution under Alkaline Conditions, ACS Applied Nano Materials, 5 (2022) 7123-7131.

[9] X. Fang, Z. Wang, S. Kang, L. Zhao, Z. Jiang, M. Dong, Hexagonal CoSe2 nanosheets stabilized by nitrogen-doped reduced graphene oxide for efficient hydrogen evolution reaction, International Journal of Hydrogen Energy, 45 (2020) 1738-1747.

[10] L. Sun, M. Gao, Z. Jing, Z. Cheng, D. Zheng, H. Xu, Q. Zhou, J. Lin, 1 T-Phase Enriched P doped WS2 nanosphere for highly efficient electrochemical hydrogen evolution reaction, Chemical Engineering Journal, 429 (2022) 132187.

[11] D. Oncel Ozgur, A novel 0D/2D/2D hetero-layered nitrogen-doped graphene/MoS2 architecture for catalytic hydrogen evolution reaction, Fuel, 328 (2022) 125538.

[12] J. Tang, C. Huang, Q. Wu, A. Cui, W. Li, Atomic-scale intercalation of N-doped carbon into monolayered MoSe2-Mo2C heterojunction as a highly efficiency hydrogen evolution reaction catalyst, Journal of Electroanalytical Chemistry, 906 (2022) 115897.

[13] S. Cogal, M. Mičušík, P. Knotek, K. Melanova, V. Zima, M. Omastová, Enhanced electrochemical performance of MoSe2 nanosheets on CoAl- layered double hydroxide for oxygen evolution reaction, Journal of Alloys and Compounds, 987 (2024) 174173.

[14] M. Saquib, N. Srivastava, P. Arora, A.C. Bhosale, NiMoSe/Ti3C2Tx MXene @ CC as a highly operative bifunctional electrocatalyst for hydrogen and oxygen evolution reactions in an alkaline medium, International Journal of Hydrogen Energy, 59 (2024) 1132-1142.

[15] K. Huang, L. Hao, Y. Liu, M. Su, Y. Gao, Y. Zhang, Facile synthesis of FeNi alloy-supported N-doped Mo2C hollow nanospheres for the oxygen evolution reaction, Journal of Colloid and Interface Science, 658 (2024) 267-275.

[16] A. Dymerska, W. Kukułka, K. Wenelska, E. Mijowska, Two-Dimensional Molybdenum Diselenide Tuned by Bimetal Co/Ni Nanoparticles for Oxygen Evolution Reaction, ACS Omega, 5 (2020) 28730-28737.

[17] Z. He, Q. Liu, Y. Zhu, T. Tan, L. Cao, S. Zhao, Y. Chen, Defect-Mediated Adsorption of Metal Ions for Constructing Ni Hydroxide/MoS2 Heterostructures as High-Performance Water-Splitting Electrocatalysts, ACS Applied Energy Materials, 3 (2020) 7039-7047.

[18] W. Ma, W. Li, H. Zhang, Y. Wang, N-doped carbon wrapped CoFe alloy nanoparticles with MoS2 nanosheets as electrocatalyst for hydrogen and oxygen evolution reactions, International Journal of Hydrogen Energy, 48 (2023) 22032-22043.

[19] M. Liu, Q. Li, X. Xiao, X. Ma, X. Xu, Y. Yin, B. Zhang, M. Ding, J. Zou, B. Jiang, CoTe2/NiTe2 heterojunction embedded in N-doped hollow carbon nanoboxes as high-efficient ORR/OER catalyst for rechargeable zinc-air battery, Chemical Engineering Journal, 486 (2024) 150256.

[20] J. Xu, J. Rong, Y. Zheng, Y. Zhu, K. Mao, Z. Jing, T. Zhang, D. Yang, F. Qiu, Construction of sheet-on-sheet hierarchical MoS2/NiS2 heterostructures as efficient bifunctional electrocatalysts for overall water splitting, Electrochimica Acta, 385 (2021) 138438.

[21] J. Kim, J.N. Heo, J.Y. Do, R.K. Chava, M. Kang, Electrochemical synergies of heterostructured Fe2O3-MnO catalyst for oxygen evolution reaction in alkaline water splitting, Nanomaterials, 9 (2019) 1486.

[22] C. Lyu, Y. Li, J. Cheng, Y. Yang, K. Wu, J. Wu, H. Wang, W.-M. Lau, Z. Tian, N. Wang, J. Zheng, Dual Atoms (Fe, F) Co-Doping Inducing Electronic Structure Modulation of NiO Hollow Flower-Spheres for Enhanced Oxygen Evolution/Sulfion Oxidation Reaction Performance, Small, 19 (2023) 2302055.

[23] J. Wang, M. Zhou, R. Fu, J. Ge, W. Yang, X. Hong, C. Sun, X. Liao, Y. Zhao, Z. Wang, Iron Molybdenum Sulfide-Supported Ultrafine Ru Nanoclusters for Robust Sulfion Degradation-Assisted Hydrogen Production, Advanced Functional Materials, n/a 2315326.

[24] J. Jiang, Y. Tian, J. Zhang, C. Zhang, L. Ai, Metallic Cu-incorporated NiFe layered double hydroxide nanosheets enabling energy-saving hydrogen generation from chlorine-free seawater electrolysis coupled with sulfion upcycling, Fuel, 367 (2024) 131506.

[25] Q. Mao, X. Mu, K. Deng, H. Yu, Z. Wang, Y. Xu, X. Li, L. Wang, H. Wang, Sulfur Vacancy-Rich Amorphous Rh Metallene Sulfide for Electrocatalytic Selective Synthesis of Aniline Coupled with Efficient Sulfion Degradation, ACS Nano, 17 (2023) 790-800.

[26] K. Gao, M. Zhou, Y. Liu, S. Wang, R. Fu, Z. Wang, J. Guo, Z. Liu, H. Wang, Y. Zhao, Q. Wang, The dual built-in electric fields across CoS/MoS2 heterojunctions for energy-saving hydrogen production coupled with sulfion degradation, Journal of Colloid and Interface Science, 657 (2024) 290-299.

[27] L. Jin, C. Chen, L. Hu, X. Liu, Y. Ding, J. He, H. Li, N. Li, D. Chen, Q. Xu, J. Lu, Ligand-induced electronic structure and morphology regulation in Ni3S2 heterostructures for efficient bifunctional electrocatalysis, Applied Surface Science, 605 (2022) 154756.

[28] W. Wang, Q. Mao, S. Jiang, K. Deng, H. Yu, Z. Wang, Y. Xu, L. Wang, H. Wang, Hetero-phase Pd4S metallene nanoribbons with Pd-rich vacancies for sulfur ion degradation-assisted hydrogen production, Applied Catalysis B: Environmental, 340 (2024) 123194.

[29] J. Huo, L. Jin, C. Chen, D. Chen, Z. Xu, C.D. Wilfred, Q. Xu, J. Lu, Improving the Sulfurophobicity of the NiS-Doping CoS Electrocatalyst Boosts the Low-Energy-Consumption Sulfide Oxidation Reaction Process, ACS Applied Materials & Interfaces, 15 (2023) 43976-43984.

[30] F. Liu, X. Cai, Y. Tang, W. Liu, Q. Chen, P. Dong, M. Xu, Y. Tan, S. Bao, Nano-Ni-Induced Electronic Modulation of MoS2 Nanosheets Enables Energy-Saving H2 Production and Sulfide Degradation, ENERGY & ENVIRONMENTAL MATERIALS, n/a e12644.